The role of defects in microwave and conventionally synthesized $LaCoO_3$ perovskite

Jesús Prado Gonjal[1], Julia Gutiérrez-Seijas[1], Irene Herrero Ansorregui[1], Emilio Morán[1], Ian Terry[2], Rainer Schmidt[3 (a)]

[1] *Universidad Complutense de Madrid, Departamento de Química Inorgánica I, Facultad de Ciencias Químicas, 28040 Madrid, Spain*

[2] *University of Durham, Department of Physics, South Road, Durham DH1 3LE, United Kingdom*

[3] *Universidad Complutense de Madrid, GFMC, Departamento Física Aplicada III, Facultad de Ciencias Físicas, 28040 Madrid, Spain*

[a)] Corresponding author. Electronic Mail: rainerxschmidt@googlemail.com

Abstract

In this work we investigate the magnetic, dielectric and charge transport properties of $LaCoO_3$ (LCO) synthesized by two different techniques: microwave assisted and conventionally heated ceramic synthesis. The rapid microwave synthesis conditions are far away from thermodynamic equilibrium and are found to lead to modified crystal defect properties as compared to conventional synthesis. Temperature (T)-dependent dielectric spectroscopy data reveal the appearance of an additional dielectric contribution that is correlated to the thermally induced magnetic spin state transition at $T_{s1} \approx 80$ K. Magnetisation, M vs T, and electrical resistivity, ρ vs T, curves reveal that the additional dielectric phase is strongly influenced by magnetic defects and may be associated with higher spin state clusters in a magnetic spin-state coexistence scenario. We suggest that defects such as oxygen vacancies act as magnetic nucleation centres across the spin state transition T_{s1} for the formation of higher spin state clusters in LCO perovskites.

Keywords: cobaltite, microwave synthesis, magnetic defects, impedance spectroscopy

1. Introduction

$LaCoO_3$ (LCO) has attracted great research interest in the past for several reasons. On the one hand, doped and undoped LCO compounds are interesting for applications in hydro-carbon oxidation exhaust catalysis [1-3], and in solid oxide fuel cells [4,5]. On the other hand, LCO is regarded a model compound for many cobaltites in terms of the thermally induced magnetic spin state transition, which has triggered a great deal of fundamental research into this compound [6-10].

The magnetic spin state transition arises due to the crystal field splitting of the octahedral Co d-electron energy levels into t_{2g} and e_g bands, where the energy gap is only marginally larger ($\approx$ 80 K) than Hund's coupling energy. This small energy difference can be overcome by thermal activation, and Co^{3+} t_{2g} electron(s) can transfer into the e_g band above the transition temperature $T_{s1} \approx 80$ K [11,12]. The compound was suggested to adopt a diamagnetic low-spin (LS) state well below T_{s1} (S = 0, $t_{2g}^6 e_g^0$) and an intermediate-spin (IS) state (S = 1, $t_{2g}^5 e_g^1$) above [13,14]. Alternatively, a high-spin (HS) state above T_{s1} has been suggested as well (S = 2, $t_{2g}^4 e_g^2$) [8,15]. Both, IS and HS models cannot correctly describe the magnetic susceptibility in LCO and a large controversy in the literature has arisen over the validity of either model. In order to reconcile such opposing views it was suggested recently that the transition may take place gradually, i.e. e_g states get populated gradually above T_{s1} and LS-IS-HS spin state coexistence may occur [16,17]. Such spin state coexistence has been predicted theoretically [18] but initial experimental evidence has been reported only recently [19].

Furthermore, the low temperature (T) defect magnetism in LCO has raised considerable research interest, where such magnetism manifests itself by a sharp upturn in the macroscopic sample magnetization upon cooling below $T \approx 30$ K. This additional magnetic structure has been associated with crystal defects such as magnetic polarons bound to oxygen vacancies and the formation of magnetic Co^{2+} [20].

In this work we study LCO powder synthesis by the use of a microwave (MW) assisted synthesis technique, which is one of the many innovative fast chemistry methods used for LCO synthesis in recent years [21-24], where rapid chemical reaction of the precursors occurs far away from thermo-dynamic equilibrium conditions [25-27]. This fast synthesis is fundamentally different from conventional (conv.) ceramic processing of precursor oxides, where in the latter the chemical reaction relies on slow particle diffusion processes across the particle boundaries of the precursor particles in thermodynamic equilibrium. In contrast to MW synthesis, the conventional synthesis of LCO has been well-established for many decades and usually does not involve any major difficulties, because LCO is known to be a stoichiometric binary oxide compound [7,28,29]. Still, the following crystal defects may typically occur in the LCO phase: (A) The presence of a certain amount of oxygen vacancies, which are compensated by partial reduction of Co^{3+} to Co^{2+} that give rise to increased electrical conductivity and a magnetic defect structure as mentioned above [30,31], and (B) small concentrations of impurity atoms inherited from the starting powders. The latter impurities can be minimized by the use of high purity starting materials.

The oxygen vacancy defects can be expected to have a distinct effect on the physical properties such as the abovementioned charge transport based on mixed valence Co^{2+}/Co^{3+} electronic conductivity and the magnetic defect mechanism based on the magnetically active Co^{2+} [20,32]. Nevertheless, the effect of defects in LCO has been scarcely studied in the literature. Therefore, the work presented here is dedicated to the investigation of defects in LCO such as the oxygen vacancies, which naturally possess different concentrations and properties inherited from the fundamentally different MW and conv. chemical synthesis routes applied in this study. In order to investigate the influence of defects on the physical properties we compare *T*-dependent magnetization (*M*) measurements and electrical impedance spectroscopy (EIS) data obtained from LCO synthesized by MW and conv. synthesis. The comparison of the physical properties

of LCO from fundamentally different chemical synthesis routes has the additional positive aspect that we have better confidence that certain physical properties observed in both types of LCO are intrinsic and inherent to the material.

From EIS data obtained from sintered ceramic pellets of both types of LCO we detect dielectric phase separation at the magnetic spin state transition T_{s1} as manifested by the appearance of an additional dielectric contribution, beyond those of the typical bulk and grain boundary (GBs) contributions in ceramic pellets. The additional dielectric phase may be associated with fractions of the sample with higher spin state (IS/HS) in a phase coexistence scenario, where magnetic and dielectric properties may be coupled via the lattice. Analysis of M vs T and electrical resistivity ρ vs T data provides evidence that the magnetic defects within LCO may act as nucleation centres for the formation of areas of higher spin states above T_{s1}.

2. Experimental methods

The LCO phase was synthesized by the relatively novel MW assisted technique [33-37], using a domestic MW oven operating at 2.45 GHz frequency and 800 W power. Equimolar amounts of precursor nitrates ($La(NO_3)_3 \cdot 6H_2O$, 99% and $Co(NO_3)_2 \cdot 6H_2O$, 98% - Sigma-Aldrich) were weighed and mixed with 5 % (wt.) of black carbon in order to enhance MW absorption. The mix was mechanically homogenized and pressed into pellets, which were placed in a small porcelain crucible situated inside another larger crucible stuffed with mullite. Phase pure LCO was obtained after 30 min of MW irradiation.

Furthermore, LCO powder was fabricated using standard conv. ceramic processing as described previously by mixing the La_2O_3 and Co_3O_4 precursor oxides and synthesis was carried out in air at 980 °C for 7 days, and the resulting product was cooled to room temperature during 6 h [19,38]. Powders from both synthesis techniques were pressed into pellet form and sintered at 1200 ºC for 24 h in air in a conventional furnace [39].

Powder X-ray diffraction (XRD) was carried out using a Philips X'Pert PRO ALPHA1 of Panalytical B.V. diffractometer with Cu Kα1 monochromatic radiation (λ=1.54056 Å) equipped with a primary curved Ge111 primary beam monochromator and a speed X'Celerator fast detector. For cell parameter measurements and phase identification the angle step and the counting time were 0.017º (2θ) and 9s, respectively. FullProf software was employed for Rietveld refinement of the XRD pattern.

Scanning electron microscopy (SEM) was carried out using a JEOL 6400 microscope operated in the secondary and backscattered electron modes on the MW synthesized powder and on sintered pellets from both MW and conv. synthesized powders. Both, powder and pellets were covered with Au by dc sputtering for SEM. Furthermore, energy dispersive spectroscopy (EDS) measurements were carried out on the sintered and thoroughly polished pellet surfaces for an area of 300 µm x 300 µm with prolonged collection time of 10 min to detect possible impurities.

Thermal gravimetry (TG) was carried out on MW synthesized powders and on crushed pellet material on a Cahn D-200 electrobalance on samples of about 80 mg in a H_2 (200 mbar)/He (400 mbar) atmosphere by heating up to 700 ºC at 6 ºC/min ramp.

M vs *T* measurements on MW and conv. synthesized LCO were performed on pellet fractions in a Quantum Design magnetic property measurement system (MPMS) operated under an applied magnetic field of 10 kOe. The samples used were rectangular prisms of about 20 mm^3 in volume and the applied magnetic field was directed along the samples' long axes. The demagnetization factors were calculated assuming a uniform magnetization from the analytical expressions given by Aharoni [40]. For both samples this leads to field corrections of about 0.03% (i.e. 0.3 mT) at 290 K, with the largest field correction being 0.1% at 2 K. In the temperature region of ≈ 80 K, where the spin state transition is expected, this field correction is between 0.03 - 0.04% for both samples.

Both sides of the LCO pellets were covered with Ag sputter deposited electrodes. EIS was carried out using an Agilent E4980A LCR meter with 100 mV amplitude of the applied ac voltage signal. The samples were placed in an Oxford Instruments sample chamber connected to an Edwards Cryodrive 1.5 closed-cycle He refrigerator. EIS data were obtained in the notation of real (Z') and imaginary (Z'') parts of the complex impedance over a wide range of frequencies (f = 10 Hz – 2 MHz) under variable temperature (T = 10 K – 320 K). Z' and Z'' values were normalized according to the pellet geometry and converted into the notations of dielectric permittivity ε'-ε'' and modulus functions M'–M'' using the standard conversion [41].

3. Results and discussion

3.1. MW synthesis aspects

High temperatures required for the synthesis of LCO crystalline material can easily be reached when cobalt-precursors are irradiated by MWs. It is well known that Co or Co_2O_3 strongly absorb MW energy and reach high temperatures quickly (≈ 700 ºC and 1300 ºC in 3 min, respectively) due to high electrical conductivity (= high dielectric losses), which results in a rapid transfer of the generated thermal energy to the reaction mixture [42,43]. In our case, the metal nitrates decompose into the respective oxides readily after starting the microwave heating. Since the metal nitrates used exhibit a perceptible degree of hydration, it can be expected that the polar character of the H_2O molecules also contributes to the strong absorption of MWs before they evaporate and concomitantly the temperature in the furnace increases rapidly at the initial stages of the synthesis process. Unfortunately it is not possible to precisely measure the reaction temperature in our domestic MW system, but the chemical reaction goes to completion and therefore the temperature may well be higher than 700 ºC. This is supported by the fact that after the 30 min of irradiation the product is still "red hot" for few seconds.

Additionally, the unproblematic MW synthesis process of LCO may be related to the excellent semi-conductivity of the final product, in contrast to other lanthanum perovskites such as $LaFeO_3$, $LaCrO_3$ or $LaAlO_3$, where an additional conventional heating step is required to obtain pure phases [36]. The first highly semi-conducting LCO clusters formed from the precursors may act in a similar way as the black carbon added as MW susceptor and scatter the subsequent MW radiation, which speeds up the reaction until completion.

3.2. Structural and microstructural characterization

Rietveld refinement of the XRD pattern of the MW synthesized LCO powder was performed initially in the R-3c space group (S.G.) and the lattice parameters were determined (Fig. 1a). The differences between observed and calculated XRD patterns are reasonably low and are indicated by the (blue) curve at the bottom of the figure. The cell parameters and atom positions are summarized in Table I and were found to be in good agreement with values in the literature [JCPDS 00-048-0123]. The fitting agreement factors were sufficiently low to indicate a good fit.

Table I: The cell parameters and atom positions from Rietveld refinements using S.G. R-3c

Cell parameters				
$\boldsymbol{a} = \boldsymbol{b}$ = 5.44366(2) Å $\boldsymbol{c}$ = 13.09569(5) Å				
Atom positions				
$LaCoO_3$ R-3c	La	0.0000	0.0000	0.2500
	Co	0.0000	0.0000	0.2500
	O	0.549(1)	0.0000	0.2500

R_p = 2.45; R_{wp} = 3.65; R_{exp} = 2.24; χ^2 = 2.67

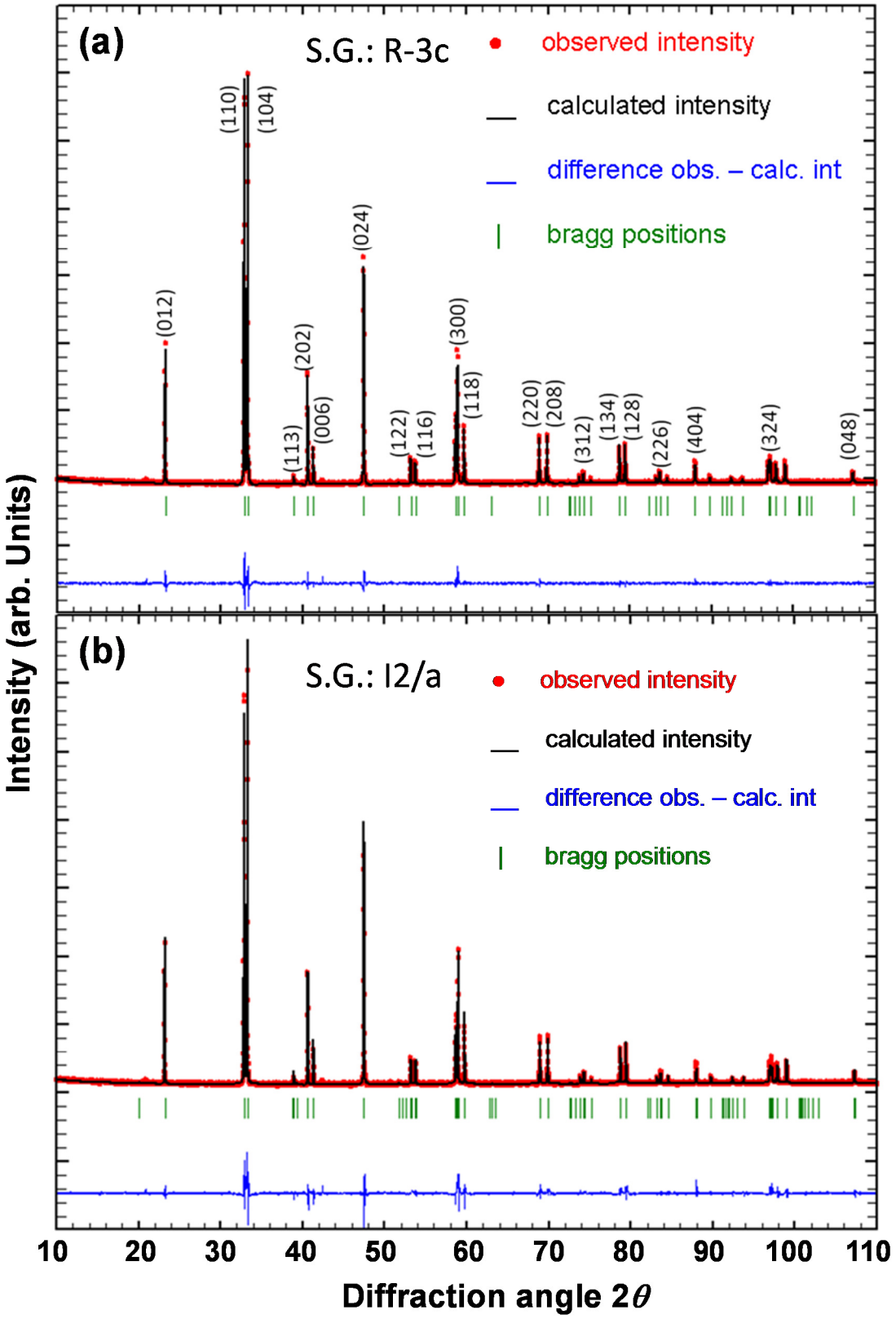

Figure 1 Rietveld fitting of powder X-ray diffraction pattern for MW synthesized LCO using **(a)** space group (S.G.) R-3c and **(b)** S.G. I2/a. Calculated and experimental intensities and their differences are shown.

It was also attempted to fit the pattern with the I2/a space group in order to account for potential monoclinic distortions, but the fitting errors were clearly higher (see Fig.1b and Table II) and we cannot confirm monoclinic distortions in our MW synthesized $LaCO_3$ system using powder XRD. Sintered pellets were analyzed by XRD as well and phase purity was confirmed within the resolution limits of XRD experiments.

Table II: The cell parameters and atom positions from Rietveld refinements using S.G. I2/a

Cell parameters				
$\boldsymbol{a}$ = 5.38081(8) Å $\boldsymbol{b}$ = 5.44126(7) Å $\boldsymbol{c}$ = 7.6539(1) Å β = 91.0144(9)°				
Atom positions				
$LaCoO_3$ I2/a	La	0.2500	0.249(1)	0.0000
	Co	0.7500	0.2500	0.2500
	O1	0.2500	-0.289(3)	0.0000
	O2	-0.0005(3)	0.011(4)	0.188(1)

$R_p = 2.98$; $R_{wp} = 4.93$; $R_{exp} = 2.34$; $\chi^2 = 4.43$

The SEM micrograph from MW synthesized LCO powder is shown in Fig.2a. Although the powder was formed only within 30 min, the average grain size of about 1μm is relatively large and no secondary phases are obvious. The pellet sintering process for the MW synthesized $LaCoO_3$ leads to increased grain size as is evident from the secondary electron SEM micrograph in Fig.2b. The pellet surface shows perceptible porosity, which may be relevant for EIS measurements. On the other hand, the contact between the grains is still satisfactory and it seems unlikely that porosity would affect the ac electrical current path significantly. Therefore, the EIS data presented below (section 3.4) may be expected to be reliable and unaffected by the porosity detected. It is interesting to note that several pores are located within single grains and not at the grain boundary areas as expected for a poorly sintered ceramic.

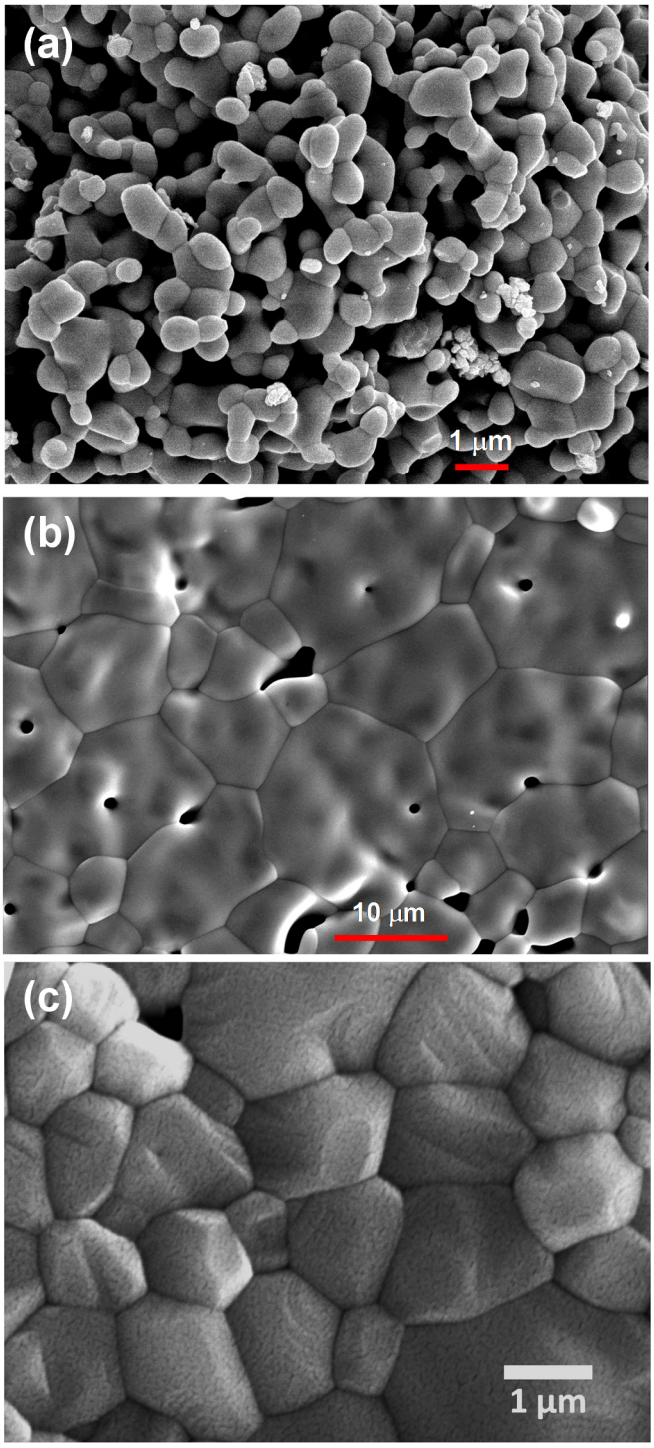

Figure 2 SEM micrograph **(a)** MW synthesized $LaCoO_3$ powder. The grain sizes are relatively uniform in the range of ≈ 1μm. **(b)** Surface of a sintered LCO pellet produced from MW synthesized LCO powder. The average grain size is in the range of ≈ 10 μm. **(c)** Surface of a sintered LCO pellet produced from conventionally synthesized LCO powder. The average grain size is in the range of ≈ 2 μm.

Sintering densification may in fact be efficient and the pores may emerge due to the carbon used for the rapid MW synthesis process, and residues of the carbon may burn out only during high temperature sintering as confirmed by the EDS analysis discussed below. Fig.2c shows a secondary electron SEM micrograph of the surface of a sintered $LaCoO_3$ pellet produced from the conv. synthesized LCO powder. The contact between the grains is satisfactory and impedance spectroscopy data is also expected to be reliable. The average grain size of the pellet from conventional synthesized LCO is smaller as compared to the MW synthesized LCO. This may well be a result of the higher sintering activity of the MW synthesized powder, which is a result of the smaller particle size in the MW powder due to the reduced MW synthesis time. The larger surface area of the MW powder enables improved diffusion processes during sintering.[44-46] It should be mentioned at this point that the ceramic microstructure may have a perceptible effect on the GB contribution in the impedance spectra, but not on the intrinsic bulk dielectric contribution and the macroscopic magnetisation data. This will be discussed in more detail in section 3.4.

The large area 10 min EDS analysis of 300 µm x 300 µm areas on the polished pellet surfaces revealed no differences between the conventionally and MW synthesized samples and no perceptible impurities or impurity phases could be detected. Quantitative analysis yielded a certain Carbon C content, which arises mainly from environmental contributions. The amount of C detected in relation with the La and Co contents was found to be 10.59% and 10.85% for the conventional and MW synthesized LCO respectively, which is the same within the EDS experimental error. We argue that significant C contamination of our LCO during the MW synthesis may be unlikely, where C was used as a MW absorber. It has been reported before that C can be doped into the lattice oxygen of $LaCoO_3$,[47,48] where it may possibly fill some oxygen vacancies. In References [47,48] the LCO was treated at a maximum of 800 °C, whereas our pellets were sintered at 1200 °C. This elevated temperature may well lead to a complete

reaction of C to CO_2 in our samples. This argument is supported by the charge transport data discussed below (section 3.4.3.). The occupation of LCO oxygen vacancies by C would be stable at high temperature only if the C is chemically bonded to the LCO crystal, in which case an increased resistivity would be expected whereas we find a smaller resistivity in the MW synthesized LCO.

The TG data presented in Fig.3 indicates approximately ideal LCO stoichiometry from the weight loss during the LCO decomposition in H_2 –rich atmosphere, which takes place in two steps:

$$2\ LaCoO_3 + H_2 \rightarrow La_2O_3 + 2\ CoO + H_2O \uparrow \quad (1a)$$

$$CoO + H_2 \rightarrow Co + H_2O \uparrow \quad (1b)$$

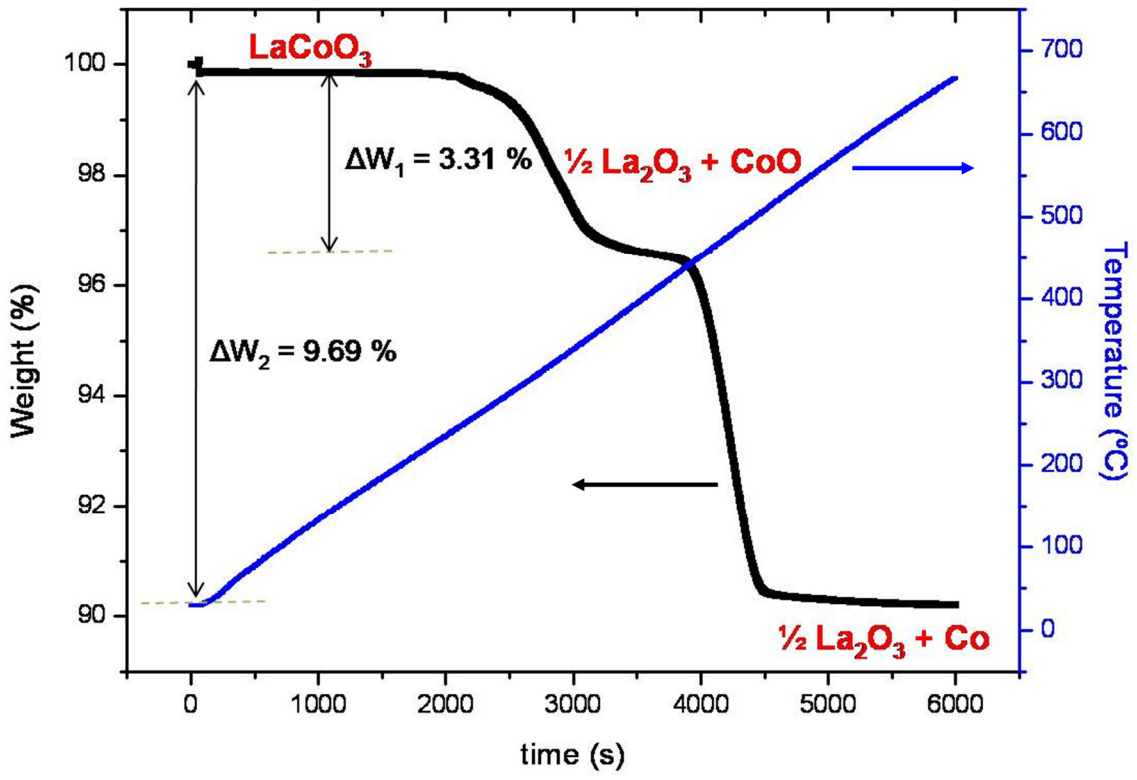

Figure 3 Thermal gravimetry (TG) of MW sintered $LaCoO_3$ powder. Weight (%) and temperature vs time in sec. The decomposition under reducing H_2 atmosphere takes place in two steps.

The weight loss measured indicates that possible oxygen vacancies in powder and pellets would exhibit a concentration below the resolution limit of the TG balance. Equivalent results were obtained from TG measurements of crushed pellet material and no indications for a significant amount of oxygen vacancies were found either. These results are in agreement with the literature, where only small amounts of oxygen vacancies in LCO have been reported [31]. For the exact determination of the oxygen vacancy concentration more sophisticated techniques such as neutron diffraction experiments would be necessary, which goes beyond the scope of the work presented here. This is a certain drawback for the comparative study presented here, because we are not able to exactly quantify the oxygen vacancy concentration directly in the two LCO phases obtained from MW and conv. synthesis. Nevertheless, a reliable measure for the oxygen vacancy concentration can be obtained indirectly from the electrical resistivity ρ, because ρ is well-known to be highly sensitive to the charge carrier density [49-51]. As demonstrated in section 3.4.3., ρ is significantly reduced in the MW synthesized LCO samples which implies a higher charge carrier concentration and higher Co^{2+} content. This is what we would expect from the much faster MW synthesis technique far away from thermo-dynamic equilibrium conditions, where a higher amount of crystal defects and oxygen vacancies would lead to higher Co^{2+} content and reduced ρ.

3.3. Magnetization vs temperature measurements

Fig.4 shows magnetization data at 10 kOe in FC mode for MW and conv. synthesized LCO in the notations of magnetization M (emu/g) on the upper panel and in terms of reciprocal susceptibility $1/\chi$ on the lower panel, both vs T. It had been shown previously that FC and ZFC measurements only vary by a small degree, which was associated with a predominantly paramagnetic nature of the magnetism [19,52]. Therefore, for simplicity only FC measurements are discussed here. The two curves for MW and conv. synthesized LCO show differences

mainly in the low-T range where the defect magnetism is evident by a sharp upturn in magnetization (upper panel) in a Curie-tail fashion upon cooling when approaching T = 0 K [18,20].

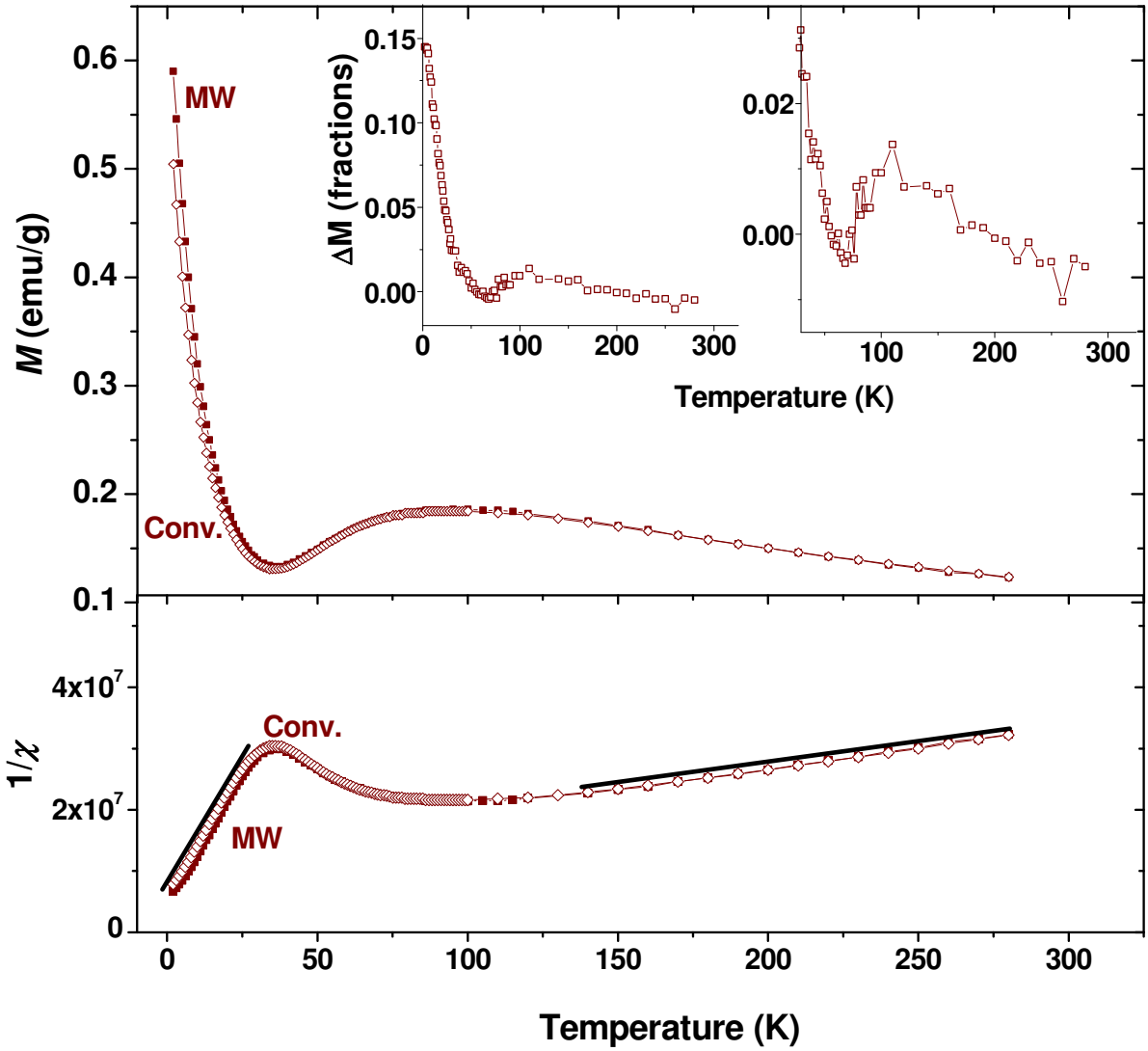

Figure 4 Field cooled (10 kOe) mass magnetization M (upper panel) and reciprocal magnetic susceptibility χ^{-1} (lower panel) vs T for MW (■) and conv. (◊) synthesized LCO. The measurement errors (not shown) are smaller than the symbols used for each data point. **Upper panel insets**: Difference of magnetization ΔM vs T. $\Delta M = (M_{mw} - M_{conv})/M_{mw/conv.}$ The right inset constitutes a magnification of the left inset near T_{s1}.

In comparison with previous work, the defect related Curie-tail appears relatively large in size in our samples here with respect to the regular magnetism. However, it should be noted that this feature does not provide a simple indication for the quality of our samples in terms of the amounts of defects. The size of the Curie-tail depends on multiple parameters such as the applied magnetic field and obviously the minimum temperature measured [52]. Nevertheless, we estimate the concentration of possible paramagnetic defects by analysing the Curie tail as described later in this section.

The difference in M for the two types of LCO was quantified in terms of ΔM [= (M_{mw} - M_{conv})/($M_{mw/conv}$)], where ΔM corresponds to the fractional difference of the magnetisation of the MW synthesized sample (M_{mw}) and the conv. synthesized sample (M_{conv}). ΔM is plotted vs T in the Fig.4 upper panel insets where $\Delta M = [(M_{mw} - M_{conv})/(M_{mw})] > 0$ in the case that the MW sample's magnetization is larger while ΔM [= (M_{mw} - M_{conv})/(M_{conv})] < 0 is used in the case that the conv. sample has the larger magnetization. This definition of ΔM was chosen in a way that ΔM is limited to $-1 < \Delta M < +1$ and is a direct measure of the magnetic differences due to the synthesis route.

The differences in the defect magnetism are clearly reflected at $T \leq 30$ K in the ΔM vs T data in in the Insets of Fig.4 and can readily be attributed to differences in concentration and/or the properties of oxygen vacancies, which are well-known to be magnetically active due to the formation of magnetic polarons [31,53]. The values of $\Delta M > 0$ at the low T-range indicate a higher amount of defects in the MW samples, which is consistent with the ρ-data (see sections 3.4.3 & 3.4.4.) suggesting a higher amount of oxygen vacancies in the MW sample. At higher temperatures the ΔM values are smaller (near zero), indicating approximately identical M vs T behaviour, except a weak additional contribution around 100 K near T_{s1} (see 2nd right-hand inset of Fig.4). The latter suggests that the defects may also play a certain role (to a different degree in the different LCO samples) near T_{s1}.

We interpret this as a first indication that magnetic defects may have an influence on the formation of the IS/HS spin-states above T_{s1}, which will be corroborated and discussed in more detail below. We argue therein that magnetic defects may serve as nucleation centres for the formation of higher magnetic spin states in the vicinity of T_{s1}, perhaps even locally modifying T_{s1} itself. Since the LCO spin state transition may involve spin-state coexistence of clusters with LS and higher spin states (IS/HS) [19], it is plausible that clusters of higher magnetic spins would form first at T_{s1} near magnetically active defects such as Co^{2+} cations coupled to the oxygen vacancies, and the clusters start to grow and nucleate at increasing temperature.

The fact that the M vs T behaviour (Fig.4) is approximately identical for $T > 150$ K for the two samples ($\Delta M \approx 0$) gives us good confidence on the precision of our measurements, and experimental errors and/or demagnetization factors do not affect the data. Note that the diamagnetic contributions from the two different LCO samples cannot be the origin of ΔM, because the diamagnetism is an intrinsic property of the LCO phase and can be assumed to be unaffected by the synthesis route, and should therefore cancel when the respective M values are subtracted. It is further pointed out that the minimum in ΔM at 60 K (Fig.4 upper panel insets) does not coincide with the minimum in M at 30 K (Fig.4 upper panel), which gives us further confidence that the features in the ΔM vs T curves cannot be experimental artefacts.

The Curie-Weiss plots of reciprocal susceptibility χ^{-1} vs T in the lower panel of Fig.4 for MW and conv. synthesized LCO show two approximately linear regimes (solid lines) as expected from the well-known Curie-Weiss law: $\chi = C/(T-\Theta)$, where C is the Curie constant and Θ is the Weiss temperature. The χ^{-1} vs T plots were differentiated to determine the strictly linear regimes, where a linear least-squares fitting routine was then employed for the low-T defect magnetism (8 – 20 K) and for the paramagnetic structure at 190 – 320 K. The fitted parameters are summarized in Tables III & IV, respectively. The slopes of the Curie-Weiss plots for the low temperature defect magnetism are larger by a factor of ≈ 10 as compared to the high

temperature paramagnetism, which highlights the different origin and the different properties of the two magnetic structures. The C values displayed in Table III for the defect magnetism for MW and conv. LCO are the same within experimental error, whereas the Θ values differ perceptibly and are both negative, ≈ -3.9 and -5.9 K respectively, indicating antiferromagnetic (AF) interactions between the magnetic defects [54].

Table III: Fitted Curie-Weiss parameters from the low-T defect magnetism (8 to 20 K):

Synthesis	C **(K)**	Θ **(K)**
Conventional	0.0412 ± 0.0002	-5.86 ± 0.06
Microwave	0.0409 ± 0.0001	-3.92 ± 0.05

An estimate of the concentration of possible paramagnetic centres (N_{pc}) related to defects in the LS diamagnetic $LaCoO_3$ matrix is obtained using the mean field expression for Curie's constant and taking a spin only value of $S \approx 13$ [54,55], we calculate a value $N_{pc} \approx 2\times10^{25}$ m^{-3}. Since the Curie constants C are the same within experimental error for MW and conv. synthesized samples, we cannot make a qualitative statement on the exact difference in the defect concentration which may be small. The estimated concentration of defects for both types of LCO may be regarded as a very low value compared to the oxygen content of $LaCoO_3$, which is supported by the fact that our samples possess relatively large ρ values as compared to previous studies as discussed below (sections 3.4.1. & 3.4.3.).

The defect magnetism has been regarded previously as a precursor to ferromagnetism (FM), which is known to be unlocked by epitaxial strain [56] or Sr hole doping [38]. Since the Θ value is slightly closer to zero for the MW sample, a weakening of the AF interactions is indicated

with a mean field interpretation suggesting that a change in the exchange energy or the mean number of nearest neighbours has taken place. As the values of the Curie constants C are approximately the same, it may be likely that the exchange energy has been reduced in the MW sample. It should be noted that the difference in Θ is likely to be responsible for the difference in M (ΔM) observed at low T ($\leq$ 30 K) in Fig.4 to some extent.

The fitted Curie-Weiss parameters for the paramagnetic structure (T > 190 K) presented in Table IV indicate that the MW sample may display weaker AF interactions, since the Weiss temperature is slightly less negative, analogous to that observed with the defect magnetism (T < 20 K). In both cases, it may be likely that the AF exchange interaction is weakened in the MW sample by local structural changes induced by the defects. It is noted that the overall regular magnetisation seems to be marginally higher in the conv. sample as indicated by a slightly higher C parameter (Table IV).

Table IV: Fitted Curie-Weiss parameters from the paramagnetic structure (190 to 320 K):

Synthesis	C **(K)**	Θ **(K)**
Conventional	0.516 ± 0.002	-175.2 ± 0.9
Microwave	0.500 ± 0.006	-163 ± 3

For completeness we should reiterate at this point that the different ceramic microstructure in the pellets produced from MW and conv. synthesized LCO powder is not expected to affect the magnetisation. Ceramic GB areas are expected to be thin and their effect may well be negligible in the magnetisation data, which are measured as a macroscopic average across the sample.

3.4. Electrical impedance spectroscopy (EIS) measurements

3.4.1. Identification of bulk and grain boundary (GB) dielectric contributions

The EIS data for MW and conv. synthesized LCO in form of sintered ceramic pellets are compared at $T = 60$ K below T_{s1} in the formats of imaginary impedance Z'' vs f (left y-axis) and imaginary modulus function M'' vs f (right y-axis) in Fig.5. This may be regarded a combined impedance and modulus spectroscopy plot [57,58]. The imaginary part of the modulus function M'' is defined as $M'' = 2\pi f C_0 Z'$, where C_0 is a constant. The Z'' vs f and M'' vs f notations and their combined plots are useful, because the two plots emphasize different features of the data.[57] Each plot displays one dielectric relaxation peak, but the difference in the peak frequencies f_{max} by ≈ two orders of magnitude indicates a different origin of the two peaks.

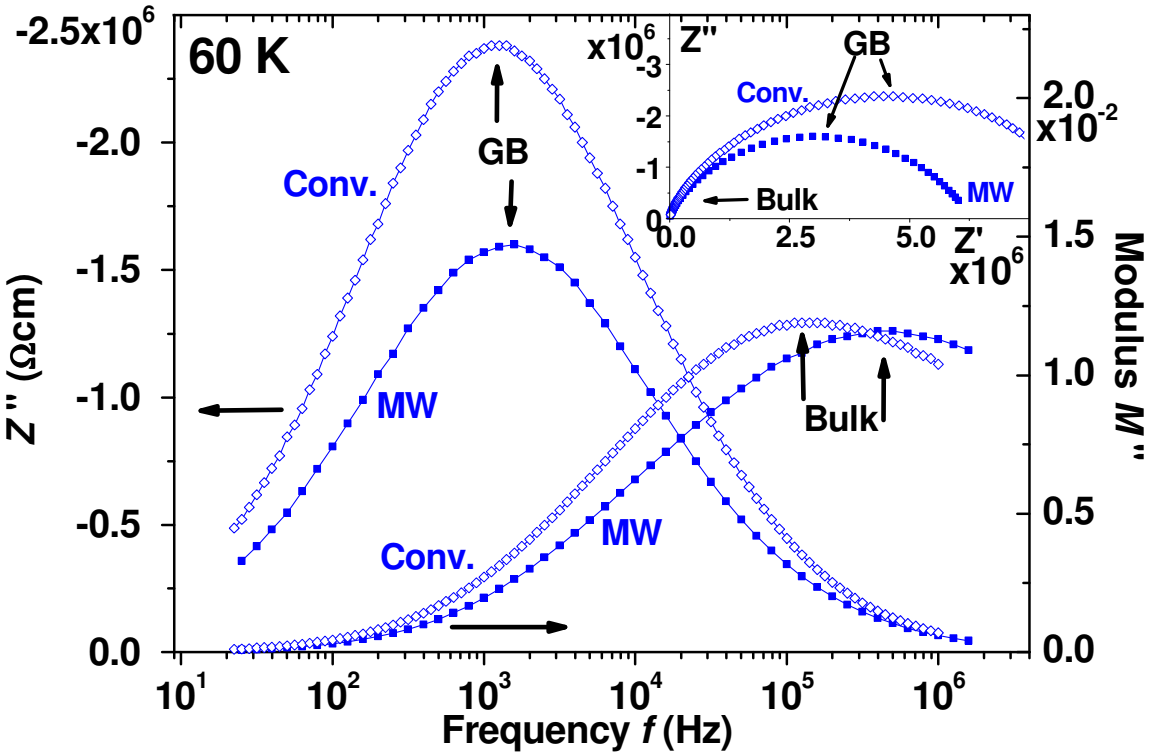

Figure 5 Imaginary impedance Z'' vs f, and modulus M'' vs f at 60 K for MW (■) and conv. (◊) LCO; GB and bulk contributions can be resolved. **Inset:** Z'' vs Z': a strong overlap of GB and bulk impedance semicircles is indicated.

The associated two dielectric contributions may originate most likely from the grain boundary (GB) and bulk areas as expected in ceramic pellets. The height of the peak in Z'' vs f is proportional to the resistance R of the associated dielectric contribution, i.e. the Z'' vs f plots are

dominated by the largest resistance in the sample, here in this case the GB resistance. On the other hand, the height of the M'' vs f peak is proportional to the reciprocal of the capacitance of the associated dielectric contribution, i.e. the M'' vs f plots are dominated by the smallest capacitance in the sample, which is the intrinsic bulk capacitance. The GB and bulk dielectric contributions must exhibit strong overlap in both types of LCO, because they cannot be resolved as separated semicircles in complex plane plots of $-Z''$ vs Z' as demonstrated in the inset of Fig.5. The typical $-Z''$ vs Z' semicircular impedance plots are dominated by the largest resistance as well, because the diameter of each semicircle corresponds to the resistance of the respective dielectric contribution. In the case of such an overlap between the GB and bulk contributions observed, the combined plots of Z'' vs f and M'' vs f may in fact be an ideal tool to achieve deconvolution of GB and bulk [57]. The dielectric peak frequencies f_{max} for GB and bulk are marked by vertical black arrows in Fig.5.

It can be seen directly that the MW synthesized sample displays a lower GB resistivity ρ, because the resistance-related and GB dominated Z'' vs f peak and the $-Z''$ vs Z' semicircle are smaller, whereas the capacitance-related M'' vs f peak is almost equivalent in height as compared to the conv. sample. This indicates that an increase in defect concentration induced by the rapid MW synthesis route leads to a considerably more conductive LCO phase, whereas significant differences in dielectric permittivity are not indicated. Apparently, defects such as oxygen vacancies mainly affect the dielectric losses of LCO samples: the decrease in ρ in the MW sample signals an increase in the concentration of oxygen vacancies, because such vacancies are compensated by Co^{2+} formation, i.e. the Co^{3+} sublattice is electron doped. The resistivity values and their differences in the two types of LCO samples were analysed quantitatively as shown below (section 3.4.3.).

3.4.2. Dielectric phase separation near the magnetic spin state transition at $T_{s1} \approx 80$ K

However, before we discuss the ρ-data it is important to notice that by heating across $T_{s1} > 80$ K, dielectric phase separation is observed by the appearance of an additional dielectric contribution associated with areas of higher spin (IS/HS), which coexists with the standard GB and bulk contributions above T_{s1} [19]. This is demonstrated in Fig.6, where the dielectric data is displayed in formats of ε' vs f (main panel) for the MW synthesized and in the notation of Z'' vs f (Fig.6 inset) for the conv. synthesized LCO. In the ε' vs f curves the phase separation at $T_{s1} \approx 80$ K is displayed at intermediate f in the form of a dip or an additional plateau in the ε' vs f curves at $T > 80$ K (the additional IS/HS phase is indicated by V symbols), in between the conv. GB and bulk ε' permittivity plateaus (solid lines) [59]. At the low frequency ends of the 120 K and 140 K curves, signs of an additional electrode sample interface effect (labelled “Electrode”) are displayed. In conv. synthesized LCO, plots of normalized Z'' vs f (Fig.6 inset) display the phase separation in form of an additional dielectric peak emerging at $T_{s1} \approx 80$ K.

Note that the additional "IS/HS" dielectric contribution may not be attributed to La_2O_3 or Co_3O_4 secondary phases for several reasons. First, the absence of secondary phases was supported by SEM and EDS analysis of the sintered pellet surfaces. Furthermore, the rather low semiconducting resistance values detected in the "IS/HS" phase (see below) are not compatible with insulating La_2O_3, or the semiconducting Co_3O_4 with high resistivity and large transport gap. Most importantly, the appearance of the "IS/HS" phase is correlated to the spin state transition at T_{s1} in both MW and conv. synthesized LCO samples.

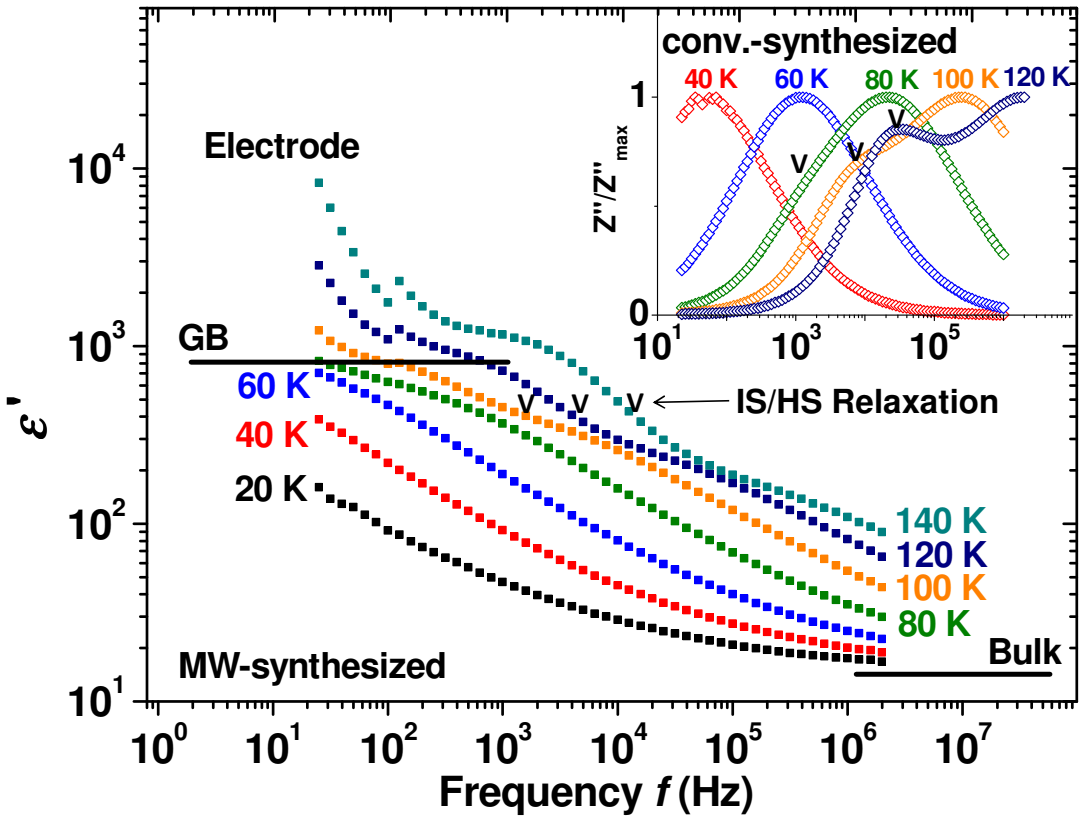

Figure 6 Dielectric permittivity ε' vs frequency f for MW synthesised LCO (■). Black solid lines represent GB and bulk plateaus. **Inset:** Normalized -Z'' vs f plots for conv. (conv.) synthesised LCO (◊). The appearance of an additional dielectric phase is indicated above $T_{s1} \approx$ 80 K by (V) markers in both notations for the two different types of LCO samples.

This dielectric phase separation at the spin state transition T_{s1} has been detected previously in conv. LCO [19], and is now confirmed in the MW synthesized species. This indicates that the concomitant coupling of magnetic and dielectric properties via the crystal lattice is an inherent and intrinsic property of the LCO perovskite phase, which agrees well with recent findings of changes in the crystal lattice strain across T_{s1} [60].

3.4.3. Resistivity vs temperature curves

The occurrence of the "IS/HS" phase implies that the direct current (dc) resistance can contain two (GB & bulk for $T < T_{s1} = 80$ K) or three components (additional "IS/HS" phase for $T > T_{s1}$

= 80 K), a feature which may explain distinct changes in the dc activation energy at T_{s1} reported previously [61]. For temperatures below 80 K in the presence of only two standard GB and bulk contributions the respective resistance values, R_{GB} and R_{bulk}, can be extracted from the spectroscopic plots readily using a standard procedure [62], using the following parameters: (A) the dielectric peak frequencies f_{max} in the Z'' vs f and M'' vs f notations, (B) the overall dc resistance $R_{dc} = R_{GB} + R_{bulk}$, (C) value of Z'' at the maximum frequency $Z''(f_{max})$, and the intrinsic bulk dielectric permittivity $\varepsilon_b \approx 16.1 \pm 0.5$ for MW synthesized and $\varepsilon_b \approx 15.7 \pm 0.5$ for conv. LCO. The bulk permittivity ε_b had been determined from the high frequency bulk permittivity plateau in the ε' vs f curves in Fig.6 (main panel). The resistance $R_{IS/HS}$ of the "IS/HS" phase above T_{s1} can be obtained by considering the dielectric peak frequency of the additional peak in Z'' vs f and $R_{dc} = R_{GB} + R_{bulk} + R_{IS/HS}$.

As mentioned before (section 3.4.2), the LCO bulk dielectric permittivity is affected only marginally by the synthesis technique and the concomitant variation in the oxygen vacancy concentration. In fact, the bulk permittivity for MW and conv. LCO are the same (16.1/15.7) within experimental error. On the other hand, the resistivity changes quite clearly, as mentioned in section 3.4.2., and therefore the role of the defects is a dispersive rather than a dielectric one. We thus focus our following discussion on the resistivity ρ values and their differences in MW and conv. synthesized LCO.

Results from the comprehensive analysis of the bulk, GB and "IS/HS" resistivity ρ in terms of the ρ-T dependencies are shown in Fig.7. The intrinsic bulk curves ρ vs T for both samples (Fig.7a) show slightly different T-trends below and above 50 K, which had been associated previously with the magnetic defect structure. The resistivity is well-known to be more strongly affected by impurities and defects at low T [19]. This finding is in agreement with different properties of the defects like their concentrations in MW and conv. synthesised LCO [31].

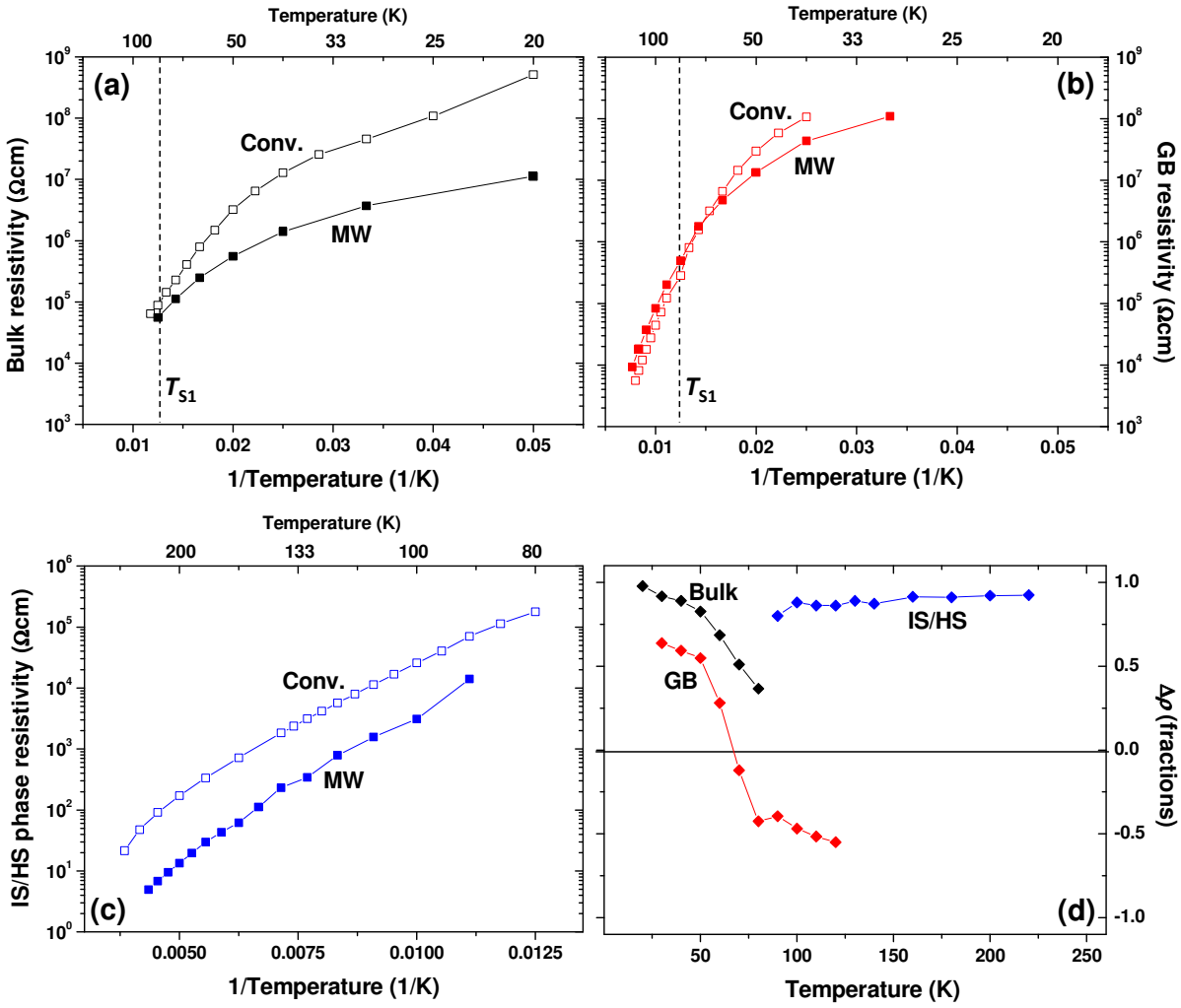

Figure 7 (**a**) Bulk, (**b**) GB and (**c**) "IS/HS" resistivity ρ vs $1/T$ for MW (■) and conv. (◊) LCO. (**d**) Fractional difference of resistivity $\Delta\rho$ vs T. $\Delta\rho = (\rho_{conv} - \rho_{mw})/(\rho_{conv/mw})$.

The GB and bulk contributions both show higher ρ for the conv. sample below T_{s1} (Fig.7b), as is the case for the "IS/HS" phase above T_{s1} (Fig.7c). On the other hand, above T_{s1} the GBs display higher ρ for the MW sample. The crossover for the GB resistivity seems to occur near T_{s1}, but it is not entirely clear whether this is indeed correlated to T_{s1}.

It should be noted at this point that the different average ceramic grain size in pellets produced from MW and conv. synthesized LCO powder may affect the GB dielectric contribution. On the other hand, the intrinsic bulk contribution is independent of the ceramic microstructure.

The absolute values of resistivity are rather high, indicating a low concentration of oxygen vacancies. At 100 K the sum of GB + bulk resistivity for the MW and conv. synthesized LCO samples can be estimated to be in the range of $\approx 10^5$ Ωcm. This is about 3 orders of magnitude higher than the resistivity reported by Aswin et al. at the same temperature [10], but in a quite similar range as the values reported by English et al. [61] and Jirak et al. [63]. Despite the relatively large magnetic Curie-tail shown above (section 3.3.), the resistivity is sufficiently high to conclude that the quality of our samples is satisfactory with a defect concentration that is low and comparable to most previous studies.

3.4.4. Differences in resistivity $\Delta\rho$

In Fig.7d the difference $\Delta\rho$ between the resistivity ρ_{mw} of the MW sample and the resistivity ρ_{conv} of the conv. sample is shown as a fraction of $\rho_{conv/mw}$ which is the resistivity of the conv. ($\Delta\rho > 0$) or the MW ($\Delta\rho < 0$) sample: $\Delta\rho = (\rho_{conv} - \rho_{mw})/(\rho_{conv/mw})$. $\Delta\rho$ is plotted vs the temperature, where the definition of $\Delta\rho$ is equivalent to ΔM (see section 3.3.). It is highlighted that the defects affect both the resistivity ρ and the magnetisation M., which is the expected behaviour of magnetically active oxygen vacancies. ΔM and $\Delta\rho$ can be regarded useful tools to detect the effects of different defect properties, although a direct correlation between the two is not obvious. Nevertheless, since $\Delta\rho$ was found to be affected by the magnetic spin state transition, it is suggested that indirect coupling of M and ρ may occur via the lattice.

$\Delta\rho$ values for the bulk are generally higher than for GBs (Fig.7), implying that the bulk is more strongly affected by the synthesis route than the GBs. Moreover, $\Delta\rho$ values for the "IS/HS" phase are relatively large (Fig.7d) which further indicates that the differences in the defect properties for MW and conv. LCO are particularly relevant to the "IS/HS" phase. This finding together with the appearance of the "IS/HS" phase at T_{s1} confirms the interpretation mentioned above (section 2.2.):

The "IS/HS" phase constitutes areas of higher spin and the transition may commence with the formation of spin droplets or clusters, which increase in number and/or size upon heating across T_{s1} in a spin-state coexistence scenario. Droplets or clusters of magnetic “IS/HS” phase areas may appear first in the proximity of oxygen vacancy defects, which act as magnetic nucleation centres. Differences in the defect properties for MW and conv. LCO may therefore lead to different magnetic nucleation behaviour at and above T_{s1}. This, in the presence of coupling between magnetic and charge transport properties, leads to differences in the resistivity of the resulting "IS/HS" phases in MW and conv. LCO.

The rather low $\Delta\rho$ values for the GBs as compared to bulk and "IS/HS" phases suggest that the GBs in the MW and conv. samples may be similar to each other, possibly due to the same air exposure during sintering of both types of pellet. The GBs may also simply exhibit generally a smaller amount of oxygen vacancies as expected in polycrystalline oxide materials where GBs are quite commonly better oxygenated.

The fractional $\Delta\rho$ values in Fig.7d are larger than ΔM (Fig.4 upper panel inset), which may well be a consequence of the high sensitivity of the method impedance spectroscopy as compared to the magnetometry applied in this work.

4. Conclusions

We conclude that the magnetic structure near the spin-state transition and the dielectric properties of MW and conv. synthesized LCO ceramics exhibit a certain dependence upon the crystal defects such as the oxygen vacancies. We propose that magnetic defects may act as nucleation centres for the gradual population of e_g levels above T_{s1}. Such gradual population of higher spin areas is reflected by the appearance of an additional dielectric phase of higher spin states (IS/HS) at the transition T_{s1}, which indicates dielectric and magnetic phase separation and coupling of dielectric and magnetic properties via the lattice. This occurs irrespective of the

synthesis technique used and thus, such observations may well reflect an intrinsic property of the perovskite LCO phase. The magnetic and, more significantly, the dielectric properties in LCO are influenced by the magnetic defect structure. We propose that the magnetic structure of LCO should be interpreted in the framework of a spin state coexistence scenario, where defects act as magnetic nucleation centres for higher spin state areas (IS/HS) within an LS matrix. Due to coupling of magnetic and charge transport properties via the lattice, changes in the magnetic defect structure are reflected in the magnetic and the charge transport properties.

Acknowledgments

R.S. wishes to acknowledge a Ramón y Cajal fellowship from the MICINN/MINECO in Spain. E.M and J.P.G. are grateful to the Comunidad Autónoma de Madrid for providing financial support (Materyener3 S2013/MIT-2753 project). The authors wish to thank Derek C. Sinclair for allowing use of the impedance spectroscopy facilities at The University of Sheffield and Neven Biskup for useful discussion.

References

[1] W. F. Libby, Science **171**, 499 (1971).
[2] R. J. H. Voorhoeve, J. P. Remeika, P. E. Freeland, and B. T. Matthias, Science **177**, 353 (1972).
[3] H. J. Hwang and M. Awano, J. Eur. Ceram. Soc. **21**, 2103 (2001).
[4] D. B. Meadowcroft, Nature **226**, 847 (1970).
[5] T. Klande, O. Ravkina, and A. Feldhoff, J. Eur. Ceram. Soc. **33**, 1129 (2013).
[6] W. C. Koehler and E. O. Wollan, J. Phys. Chem. Solids **2**, 100 (1957).
[7] J. B. Goodenough, J. Phys. Chem. Solids **6**, 287 (1958).
[8] M. Magnuson, S. M. Butorin, C. Såthe, J. Nordgren, and P. Ravindran, EPL **68**, 289 (2004).
[9] R. F. Klie, J. C. Zheng, Y. Zhu, M. Varela, J. Wu, and C. Leighton, Phys. Rev. Lett. **99**, 047203 (2007).
[10] V. Aswin, P. Kumar, P. Singh, A. Gupta, S. Rayaprol, and A. Dogra, J. Mater. Sci. **50**, 366 (2015).
[11] K. Knizek, Z. Jirak, J. Hejtmanek, P. Novak, and W. Ku, Phys. Rev. B **79**, 014430 (2009).
[12] K. Knížek, Z. Jirák, J. JHejtmánek, and P. Novák, J. Phys. Condens. Matter **18**, 3285 (2006).
[13] M. A. Korotin, S. Y. Ezhov, I. V. Solovyev, V. I. Anisimov, D. I. Khomskii, and G. A. Sawatzky, Phys. Rev. B **54**, 5309 (1996).
[14] A. Ishikawa, J. Nohara, and S. Sugai, Phys. Rev. Lett. **93**, 136401 (2004).
[15] G. H. Jonker, J. Appl. Phys. **37**, 1424 (1966).
[16] D. P. Kozlenko, N. O. Golosova, Z. Jirak, L. S. Dubrovinsky, B. N. Savenko, M. G. Tucker, Y. L. Godec, and V. P. Glazkov, Phys. Rev. B **75**, 064422 (2007).
[17] K. Asai, A. Yoneda, O. Yokokura, J. M. Tranquada, G. Shirane, and K. Kohn, J. Phys. Soc. Jpn. **67**, 290 (1998).
[18] E. L. Nagaev and A. I. Podelshchikov, J. Phys. Condens. Matter **8**, 5611 (1996).
[19] R. Schmidt, J. Wu, C. Leighton, and I. Terry, Phys. Rev. B **79**, 125105 (2009).
[20] S. R. Giblin, I. Terry, S. J. Clark, T. Prokscha, D. Prabhakaran, A. T. Boothroyd, J. Wu, and C. Leighton, EPL **70**, 677 (2005).
[21] L. Predoana, B. Malic, D. Crisan, N. Dragan, M. Anastasescu, J. Calderon-Moreno, R. Scurtu, and M. Zaharescu, Ceram. Internat. **38**, 5433 (2012).
[22] L. Predoana, A. Jitianu, B. Malic, and M. Zaharescu, J. Am. Ceram. Soc. **95**, 1068 (2012).
[23] L. Predoana, B. Malic, M. Kosec, M. Carata, M. Caldararu, and M. Zaharescu, J. Eur. Ceram. Soc. **27**, 4407 (2007).
[24] M. Popa and J. M. Calderon-Moreno, J. Eur. Ceram. Soc. **29**, 2281 (2009).
[25] F. S. Al-Hazmi and W. E. Mahmoud, J. Eur. Ceram. Soc. **34**, 3047 (2014).
[26] A. Al-Alas, S. Beg, N. A.S.Al-Areqi, and S. Hafeez, J. Eur. Ceram. Soc.**33**, 2111 (2013).
[27] J. Prado-Gonjal, R. Schmidt, J.-J. Romero, D. Ávila, U. Amador, and E. Morán, Inorg. Chem. **52**, 313 (2013).
[28] R. R. Heikes, R. C. Miller, and R. Mazelsky, Physica **30**, 1600 (1964).
[29] M. A. Señarís-Rodríguez and J. B. Goodenough, J. Solid State Chem. **116**, 224 (1995).
[30] V. V. Kharton, F. M. Figueiredo, A. V. Kovalevsky, A. P. Viskup, E. N. Naumovich, A. A. Yaremchenko, I. A. Bashmakov, and F. M. B. Marques, J. Eur. Ceram. Soc. **21**, 2301 (2001).
[31] P. G. Radaelli and S. W. Cheong, Phys. Rev. B **66**, 094408 (2002).

[32] E. Iguchi, K. Ueda, and W. H. Jung, Phys. Rev. B **54**, 17431 (1996).
[33] M. Panneerselvam and K. J. Rao, J. Mater. Chem. **13**, 596 (2003).
[34] Y. S. Malghe, A. V. Gurjar, and S. R. Dharwadkar, J. Therm. Anal. Calorim. **78**, 739 (2004).
[35] S. Farhadi and S. Sepahvand, Journal of Alloys and Compounds **489**, 586 (2010).
[36] J. Prado-Gonjal, Á. M. Arévalo-López, and E. Morán, Mater. Res. Bull. **46**, 222 (2011).
[37] J. Prado-Gonjal, R. Schmidt, and E. Morán, in *Perovskite: Crystallography, Chemistry and Catalytic Performance*, edited by J. Zhang, and H. Li (Nova Science Pub Incorporated, 2012), pp. 117.
[38] J. Wu and C. Leighton, Phys. Rev. B **67**, 174408 (2003).
[39] K. Kleveland, M. A. Einarsrud, and T. Grande, J. Eur. Ceram. Soc. **20**, 185 (2000).
[40] A. Aharoni, J. Appl. Phys. **83**, 3432 (1998).
[41] E. Barsukov and J. Macdonald, *Impedance Spectroscopy: Theory, Experiment and Applications* (John Wiley & Sons Inc., Hoboken, 2005).
[42] K. J. Rao, B. Vaidhyanathan, M. Ganguli, and P. A. Ramakrishnan, Chem. Mater. **11**, 882 (1999).
[43] D. M. P. Mingos and D. R. Baghurst, Chem. Soc. Rev. **20**, 1 (1991).
[44] J. Prado-Gonjal, R. Schmidt, J. Espíndola-Canuto, P. Ramos-Alvarez, and E. Morán, J. Power Sources **209**, 163 (2012).
[45] J. Prado-Gonjal, R. Heuguet, D. Muñoz-Gil, A. Rivera-Calzada, S. Marinel, E. Morán, and R. Schmidt, Int. J. Hydrogen Energy **40**, 15640 (2015).
[46] N. P. Bansal and A. R. Boccaccini, *Ceramics and Composites Processing Methods* (John Wiley & Sons, Inc., Hoboken (USA), 2012).
[47] L. Jia, J. Li, W. Fang, H. Song, Q. Li, and Y. Tang, Catal. Commun. **10**, 1230 (2009).
[48] L. Jia, J. Li, and W. Fang, Catal. Commun. **11**, 87 (2009).
[49] N. Tsuda, K. Nasu, A. Fujimori, and A. Siratori, *Electronic Conduction in Oxides* (Springer, Berlin, 2002), Solid-State Sciences.
[50] R. Schmidt, A. Basu, and A. W. Brinkman, Phys. Rev. B **72**, 115101 (2005).
[51] B. I. Shklovskii and A. L. Efros, *Electronic properties of doped semiconductors* (Springer, Berlin, 1984), Solid State Sci. 45.
[52] S. R. Giblin, University of Durham, 2006.
[53] N. Biskup, J. Salafranca, V. Mehta, M. P. Oxley, Y. Suzuki, S. J. Pennycook, S. T. Pantelides, and M. Varela, Phys. Rev. Lett. **112**, 087202 (2014).
[54] S. R. Giblin, I. Terry, D. Prabhakaran, A. T. Boothroyd, and C. Leighton, Phys. Rev. B **79**, 174410 (2009).
[55] S. Yamaguchi, Y. Okimoto, H. Taniguchi, and Y. Tokura, Phys. Rev. B **53**, R2926 (1996).
[56] J. W. Freeland, J. X. Ma, and J. Shi, Appl. Phys. Lett. **93**, 212501 (2008).
[57] J. T. S. Irvine, D. C. Sinclair, and A. R. West, Adv. Mater. **2**, 132 (1990).
[58] A. R. West, T. B. Adams, F. D. Morrison, and D. C. Sinclair, J. Eur. Ceram. Soc. **24**, 1439 (2004).
[59] R. Schmidt, J. Ventura, E. Langenberg, N. M. Nemes, C. Munuera, M. Varela, M. Garcia-Hernandez, C. Leon, and J. Santamaria, Phys. Rev. B **86**, 035113 (2012).
[60] Z. Zhang, J. Koppensteiner, W. Schranz, D. Prabhakaran, and M. A. Carpenter, J. Phys. Condens. Matter **23**, 145401 (2011).
[61] S. R. English, J. Wu, and C. Leighton, Phys. Rev. B **65**, 220407 (2002).
[62] R. Schmidt and D. C. Sinclair, Chem. Mater. **22**, 6 (2010).
[63] Z. Jirak, J. Hejtmanek, K. Knizek, and M. Veverka, Phys. Rev. B **78**, 014432 (2008).